

ARTICLE OPEN

Topological defects at octahedral tilting plethora in bi-layered perovskites

Fei-Ting Huang¹, Bin Gao¹, Jae-Wook Kim¹, Xuan Luo², Yazhong Wang¹, Ming-Wen Chu³, Chung-Kai Chang⁴, Hwo-Shuenn Sheu⁴ and Sang-Wook Cheong^{1,2}

Oxygen octahedral distortions, including tilts/rotations, deformations and off-centring in (layered) perovskites, have the key role in their numerous functional properties. Near the polar-centrosymmetric phase boundary in bi-layered perovskite $\text{Ca}_{3-x}\text{Sr}_x\text{Ti}_2\text{O}_7$ with $x \approx 1$, we found the presence of abundant topological eight-state vortex-antivortex pairs, associated with four oxygen octahedral tilts at domains and another four different oxygen octahedral tilts at domain walls. Our discovery opens a new revenue to unveil real-space topological defects associated with the possible vector choices in one specific lattice mode.

npj Quantum Materials (2016) 1, 16017; doi:10.1038/npjquantmats.2016.17; published online 7 October 2016

INTRODUCTION

Copious functional phenomena, including high T_c superconductivity,¹ ferroelectricity,^{2,3} novel magnetism^{4–6} and giant photovoltaic effects,^{7,8} have been observed in perovskite (ABO_3)-related compounds, where those physical properties can be closely associated with oxygen octahedral distortions, including tilts/rotations, deformations and off-centring. For example, the high carrier mobility in transparent conducting cubic BaSnO_3 (ref. 9) or photovoltaic halide perovskites^{9,10} is closely related with (nearly) 180° bonding between large B-site cations and an oxygen (or a halide ion), resulting from little octahedral distortions. Even when A-site ions are rather small, the perovskite-related structure can be still stabilised through oxygen octahedral tilts/rotations.¹¹ It turns out that superconductivity in $(\text{La},\text{Ba})_2\text{CuO}_4$ is significantly influenced by oxygen octahedral tilts,^{12,13} and canted magnetic moments appear in antiferromagnetic perovskites with tilted/rotated oxygen octahedra through Dzyaloshinskii–Moriya interaction.^{2,14} High dielectric response in the vicinity of the morphotropic phase boundary is a consequence of the continuously rotating polarisation with various octahedral tilts.^{15,16} Crystal field split can be considerably influenced by compression or elongation of oxygen octahedra, which is the origin of the Jahn–Teller effects for $\text{B} = \text{Cu}^{2+}$ or Mn^{3+} (refs 1,17,18).

Remarkably, the simultaneous presence of oxygen octahedral tilt and rotation can result in ferroelectric polarisation in perovskites with even number of layers, which is called hybrid improper ferroelectricity.^{19–21} It has experimentally verified that bi-layered perovskite $\text{Ca}_{3-x}\text{Sr}_x\text{Ti}_2\text{O}_7$ (CSTO) is a hybrid improper ferroelectric with switchable polarisation of $8 \mu\text{C cm}^{-2}$ in bulk crystals at room temperature.²⁰ Ferroelectricity in CSTO described by a hybridisation of two structural modes (octahedral tilt and rotation modes) turns out to be associated with an intriguing domain topology consisting of $Z_4 \times Z_2$ domains and Z_3 vortices with eight domains (four directional domains and two antiphase domains), abundant charged domain walls and unique zipper-like switching kinetics.²² In $Z_4 \times Z_2$ domains, Z_4 denotes the cyclic group of order 4 for directional variants and Z_2 is for translational

variants. In this article, utilising *in situ* heating transmission electron microscopy (TEM) studies, synchrotron powder X-ray diffraction experiments and dielectric measurements, we report the discovery of a new intermediate tetragonal state in CSTO, which demonstrates a displacive nature of hybrid improper ferroelectricity mechanism different from those predicted from the group–subgroup relation.^{21,23} Furthermore, we find the presence of topological eight-state vortex–antivortex defects associated with two-dimensional eight degrees of freedom for oxygen octahedral tilts in the intermediate tetragonal state.

RESULTS

Figure 1 depicts the possible octahedral tilts/rotations in bi-layered perovskite CSTO, resulting in different structural states and also domains with different directional order parameters. For each space group, the distortion axes and the corresponding Glazer notations²⁴ are given with respect to the un-distorted tetragonal $I4/mmm$ (T) structure (Figure 1b). The term ‘rotation’ denotes a rotation of the basal oxygen plane around the $[001]_T$ axis in a clockwise (+) or counterclockwise (–) manner (Figure 1c for +). Out-of-phase and in-phase rotation in adjacent layers within one bi-layered perovskite block lead to orthorhombic O^* and O' states, respectively. Note that the presence of an intermediate O^* state (Figure 1c) competing with the ground-state polar O state, responsible for uniaxial negative thermal expansion, has been confirmed in hybrid improper ferroelectricity magnet $\text{Ca}_3\text{Mn}_2\text{O}_7$ (refs 25, 26). The term ‘tilt’ is associated with a tilt around an in-plane axis, and it would move the basal oxygens out of the basal plane and the apical oxygen away from the c axis. In-plane tilting axes can be along $\langle 110 \rangle_T$ and $\langle 100 \rangle_T$ directions, leading to orthorhombic O' (Figure 1e) and tetragonal T' states (Figure 1f), respectively. Following the Glazer notation, the T state has the $a^0a^0c^0$ pattern and the T' , O' , O^* and O'' states are described as $a^-a^0c^0$, $a^-a^-c^0$, $a^0a^0c^-$ and $a^0a^0c^+$, respectively. Two end members, $\text{Sr}_3\text{Ti}_2\text{O}_7$ and $\text{Ca}_3\text{Ti}_2\text{O}_7$, correspond to two extremes: the un-distorted T state of $\text{Sr}_3\text{Ti}_2\text{O}_7$ and the O state with both tilt

¹Rutgers Center for Emergent Materials and Department of Physics and Astronomy, Rutgers University, Piscataway, New Jersey, USA; ²Laboratory for Pohang Emergent Materials and Max Plank POSTECH Center for Complex Phase Materials, Pohang University of Science and Technology, Pohang, Korea; ³Center for Condensed Matter Sciences, National Taiwan University, Taipei, Taiwan and ⁴National Synchrotron Radiation Research Center, Hsinchu, Taiwan.

Correspondence: S-W Cheong (sangc@physics.rutgers.edu)

Received 10 June 2016; revised 27 July 2016; accepted 16 August 2016

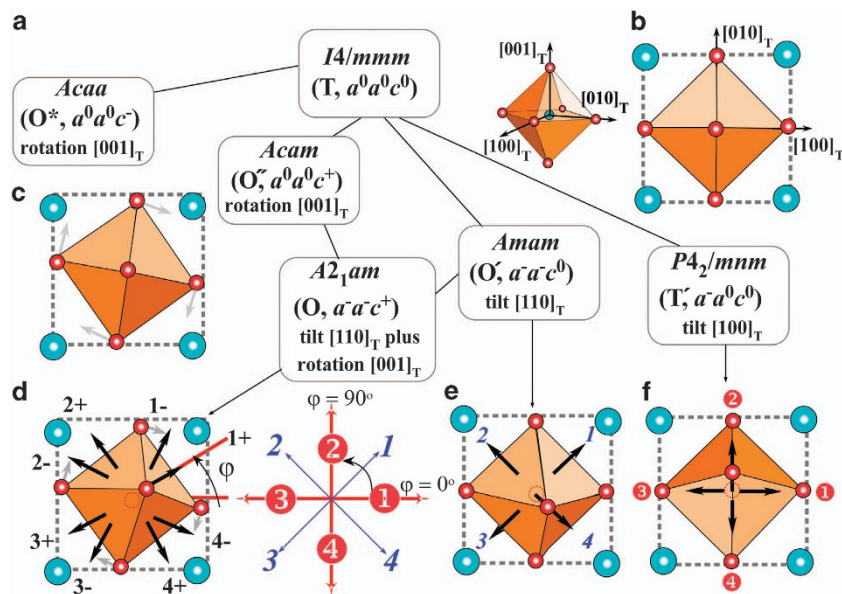


Figure 1. (a) Schematic diagram of possible space groups and the corresponding Glazer notations for bi-layered perovskite $A_3B_2O_7$. Lines link the group–subgroup relations. The lattice directions are given with respect to the T state ($I4/mmm$). (b–f) In-plane projected views of various BO_6 octahedral tilts/rotations. The dashed lines outline the primitive unit cells, and the red and cyan spheres represent the O and B-site ions, respectively. Black and gray arrows indicate directions of apical and basal plane oxygen displacements, respectively. (b) Un-distorted BO_6 octahedron in the T state. (c) A clockwise (+) rotated BO_6 in the O^* and O' states. The rotation can be also counterclockwise (–). In two adjacent layers within one bi-layer, an out-of-phase rotation (+ – or – +) along the c axis occurs in the O^* state while in-phase (+ + or – –) rotation in the O' state. (d) Eight possible $1\pm$, $2\pm$, $3\pm$ and $4\pm$ apical oxygen displacements in the O state. The azimuthal angle, φ , of an apical oxygen distortion is denoted. (e) Given tilting vectors in the O' state. (f) Four possible apical oxygen displacements (red-circled labels) along the $\langle 100 \rangle_T$ directions in the T' state.

and rotation ($a^-a^-c^+$) of $Ca_3Ti_2O_7$ (Figure 1d). It is clear why orthorhombic O' ($a^-a^-c^0$) and O'' ($a^0a^0c^+$) states are the two plausible intermediate structures toward the polar O structure ($a^-a^-c^+$) by symmetry.^{21,23} With the underlying square lattice, various symmetry-equivalent domains may exist in each of those states. It is convenient to define the azimuthal angle of an apical oxygen distortion, φ , as shown in Figure 1d. This φ links all possible directions of apical oxygen motions among those phases; for example, symmetry-equivalent domains of the T' phase correspond to $\varphi = 0^\circ, 90^\circ, 180^\circ$ and 270° (red-circled ①, ②, ③ and ④ in Figure 1f, respectively), whereas those in the O' phase to $\varphi = 45^\circ, 135^\circ, 225^\circ$ and 315° (blue, 1, 2, 3 and 4 in Figure 1e, respectively). The domains of the polar O state has $\varphi = 45^\circ \pm \alpha, 135^\circ \pm \alpha, 225^\circ \pm \alpha$ and $315^\circ \pm \alpha$, where α depends on the sign and magnitude of octahedral rotation ($a^0a^0c^+$; $1\pm, 2\pm, 3\pm$ and $4\pm$ in Figure 1d, respectively).

We have performed synchrotron powder X-ray diffraction experiments using the collimated synchrotron-radiation beam with the wavelength of 0.688 Å at the National Synchrotron Radiation Research Center, Taiwan. Homogeneous and phase-pure polycrystalline CSTO ($0 \leq x \leq 3$) specimens were prepared by a solid-state reaction method (Materials and methods). The general structure analysis system program using the Rietveld method with a pseudo-Voigt profile function was exploited to analyse the powder diffraction data. The evolution of octahedral rotation (θ_R) and tilting (θ_T) angles of TiO_6 , and lattice parameters a , b and c as a function of Sr content, x , is summarised in Figure 2a and Supplementary Figure S1a. The phase diagram, constructed from these structural parameters, consists of ferroelectric O (purple, $0 \leq x \leq 0.9$) and paraelectric T states (pink, $x \geq 1.5$). The asymmetric decays of θ_R and θ_T at $x = 0.915-1$ defines a sharp and narrow region with only non-zero θ_T (yellow, Figure 2a). The high-resolution X-ray diffraction data clearly display peak splitting only when $x \leq 0.9$, implying a tetragonal symmetry in this narrow

region (Supplementary Figure S1b). A $\sqrt{2} \times \sqrt{2}$ supercell in electron diffraction patterns from TEM (Figure 2c) is found for $x = 0.915-1$, confirming the stabilisation of a new tetragonal intermediate state distinct from the parent T state. The Rietveld refinement of synchrotron data provides further confirmation of the existence of the T' state with the $a^-a^0c^0$ pattern (Supplementary Figure S1c). The details of X-ray refinement fits are given in Supplementary Section 1 and Supplementary Table S1. The dielectric constant also shows a marked change in magnitude upon entering the T' state and displays almost two times larger epsilon (ϵ) value at the phase boundary of $x = 0.9$, compared with that of low x values (Figure 2b). An increase in ϵ at 350 K can be understood as increasing structural fluctuations when approaching from the ferroelectric O to paraelectric T' states. Indeed, *in situ* TEM heating experiments of $Ca_{2.1}Sr_{0.9}Ti_2O_7$ crystals exhibit a two-step transformation upon heating: $O \rightarrow T' \rightarrow T$. Figure 2c shows first that the intensity of superlattice S_1 -type spots $\frac{1}{2}(130)_T$ of the O state (cyan triangles) weakens as temperature (T , defined italic T as temperature) is raised from 300 to 450 K. Two additional sets of superlattice S_2 -type $\frac{1}{2}(200)_T$ and S_3 -type $\frac{1}{2}(\bar{1}30)_T$ spots (yellow and green triangles), corresponding to the T' state, appear when temperature is further raised to 473 K. Finally, all superlattice spots vanish above 713 K. Thus, we have demonstrated the stabilisation of the intermediate T' state by varying chemical composition as well as temperature. Starting from the O state at low x , Figure 2a shows a faster relaxation of the octahedral rotation (θ_R) than that of tilting (θ_T) with increasing Sr doping, which is also coupled with an increasing trend of orthorhombicity.²⁰ The sudden suppression of octahedral rotations occurs when the azimuthal angle φ suddenly switches from $\sim 45^\circ$ at $x = 0.9$ to 0° in the T' state (Figure 1a), indicating a likely discontinuous change of the tilting order parameter and a first-order phase transition. Note that we do not observe any evidence for an intermediate

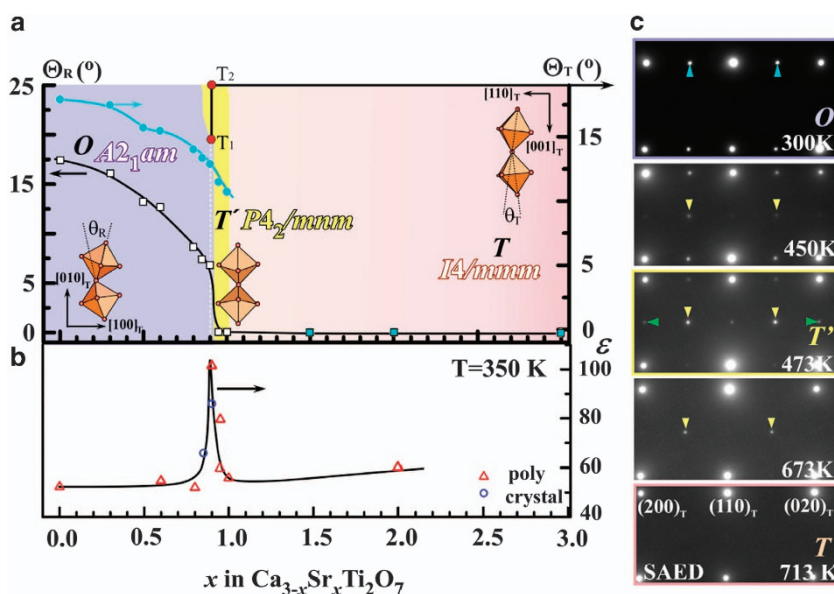


Figure 2. (a) Structural phase diagram of $\text{Ca}_{3-x}\text{Sr}_x\text{Ti}_2\text{O}_7$ with the angles of octahedral rotation (θ_R , empty squares) and tilt (θ_T , cyan spheres) as a function of Sr doping, x . The black and cyan curves are guides for the eyes. Two structural phase transition temperatures ($T_1 = 473$ K and $T_2 = 710$ K) at $x = 0.9$, marked with red spheres, are obtained from *in situ* TEM heating experiments. (b) Dielectric constant versus Sr content (x), measured at 350 K and 44 kHz. Red triangles and blue circles are from measurements on polycrystalline and single-crystalline (electric field applied along the in-plane direction) specimens, respectively. The dielectric constant peaks at the O–T' structural boundary of $x = 0.9$. (c) Thermal sequence of selected area electron diffraction patterns on $x = 0.9$, showing two phase transitions upon *in situ* heating: O (300 K) \rightarrow T' (473 K) \rightarrow T (713 K) states. $S_1 = \frac{1}{2}(130)_T$ -type superlattice spots (cyan triangles) are allowed in the O state. When temperatures reaches 473 K, additional $S_2 = \frac{1}{2}(200)_T$ -type and $S_3 = \frac{1}{2}(-130)_T$ -type superlattice spots appear (yellow and green triangles), indicating the appearance of a tetragonal T' state. Above 713 K, all superlattice spots disappear, consistent with the presence of the T state at very high temperatures.

O' ($a^-a^-c^0$, $\varphi = 45^\circ$) state, reported in the solid solution of $\text{Ca}_3\text{Ti}_2\text{O}_7$ -(Ca,Sr) $_{1.15}\text{Tb}_{1.85}\text{Fe}_2\text{O}_7$ (ref. 27).

Figures 3a and b show a $2.7 \times 1.7 \mu\text{m}$ mosaic of dark-field (DF) TEM images of the T' state $x = 0.95$ taken using S_2 spot (red circle in Figure 3b) and its corresponding diffraction pattern along the $[001]_T$ direction. The curved dark-contrast lines reveal boundaries of four T'-phase domains merging at one core, which is a non-T' state. With the underlying square lattice, 4 symmetry-equivalent domains, named $Z_1 \times Z_4$ domains, may exist; four translational variants associated with the translation vectors $(\frac{1}{2}, \frac{1}{2}, 0)$, $(0, \frac{1}{2}, \frac{1}{2})$ and $(\frac{1}{2}, 0, \frac{1}{2})$ where out-of-plane phase shifts are involved in the latter two. However, the domain topology can be renamed as $Z_2 \times Z_2$ domains when the in-plane order parameters (octahedral tilts) of one bilayer is considered; two directional variants ($[010]_T$ -tilt producing ①/③ and $[100]_T$ -tilt producing ②/④) and two translational variants associated with the in-plane translation vector $(\frac{1}{2}, \frac{1}{2}, 0)$ between ①–③ and ②–④ (Figure 1f). Our results demonstrate that four domains, corresponding to red-circled ①, ②, ③ and ④ in Figure 1f, form an exclusive vortex-like pattern with 90° -rotating apical oxygen distortions (red arrows in Figure 3a). These four domains are represented by four values of apical oxygen azimuthal angles $\varphi = 0^\circ, 90^\circ, 180^\circ$ and 270° ; for example, domains ① and ③ correspond to $\varphi = 0^\circ$ and 180° , respectively. Note that the domain network (Figure 3a) can be described by two proper colouring, i.e., two colours is sufficient to identify the domains without neighbouring domains sharing the same colour (white and green in Supplementary Figure S3a), and the vortex network can be constructed by cutting through two types of closed loops (blue and light blue in Supplementary Figure S3a) based on a graph-theoretical description.²⁸ Intriguingly, those curved domain walls exhibit two distinct extinction rules in the superlattice DF-TEM images. Figure 3c shows a DF-TEM image using a S_1 spot (light-blue circled in Figure 3b), revealing only a

part of domain walls. A complementary domain-wall map is obtained using a S_3 spot for DF-TEM imaging (blue-dotted circled in Figure 3b). The inequivalent nature of these two DF-TEM images with different superlattice peaks with ab plane components indicates an orthorhombic-like local structure at those walls, instead of, e.g., a high-symmetry T state. Considering a pure tilting nature of the matrix T' state and the distinct extinction rules, those domain walls are likely in the O' state (Figure 1e). The directions of oxygen octahedral tilts and apical oxygen distortions are denoted as light blue and blue arrows in the Figures 3c and d insets, respectively—more details are discussed in Supplementary Section 2. Therefore, oxygen octahedra inside the bright-contrast domains tilt along either $[100]_T$ or $[010]_T$ directions whereas those in the dark-contrast domain walls tilt along diagonal $\langle 110 \rangle_T$ directions. The full assignment of vortices and antivortices in Figure 3a is given in Supplementary Figures S3a and b, based on the structural information derived from Figures 3c and d. This leads to a unique Z_4 vortex structure with four domains and four domain walls, where oxygen octahedra tilt and φ changes by 45° consecutively around the vortex core. The Z_4 vortex consists of four phases of domains and also four other phases at domain walls allowed with X_3^- mode representation of octahedral tilts, whereby the tilting axes and amplitude are specified by the order parameter direction. The relevant order parameter directions are (a, a) for the T'-state and $(a, 0)$ for the O'-state, where the value a corresponds to the magnitude of tilt around the x and y axes.²⁹ Indeed, those domain walls show a finite width of ~ 7 – 9 T'-unit cells as estimated from a scanning TEM image (yellow-shaded area in Figure 3e), which is much thicker than that of atomically sharp domain walls found in proper ferroelectrics such as in $\text{Pb}(\text{Zr}_{0.2}\text{Ti}_{0.8})\text{O}_3$ (ref. 30). The structural model superimposed in Figure 3e corresponds to one projected unit cell (blue: Ca/Sr; green: Ti; grey: Sr; and red: O). The A-site

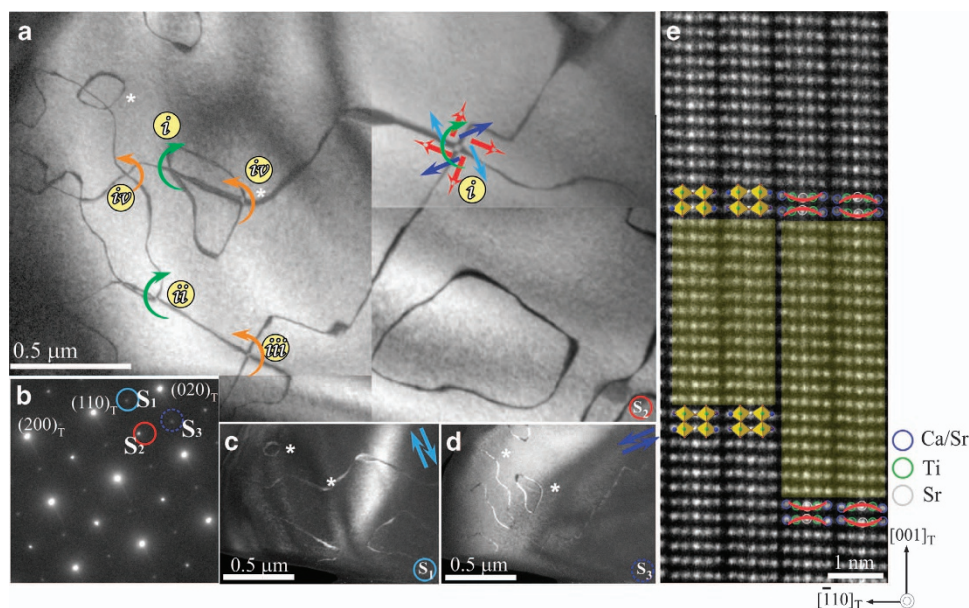


Figure 3. (a) A $2.7 \times 1.7 \mu\text{m}$ mosaic of DF-TEM images, taken using a superlattice S_2 spot (red circled) in a CSTO $x=0.95$ specimen along the $[001]_T$ direction. The coloured arrows represent octahedral tilting directions; red arrows for four phases of domains in the T' state and (light)-blue arrows for four phases of domain walls in the O' state. Yellow-circled $i-iv$ are Z_4 vortex-antivortex defects. Asterisks are location markers. (b) The corresponding selected area electron diffraction. (c) A superlattice DF-TEM image, taken using a superlattice S_1 spot (light blue-circled), exhibits only a part of domain walls in a. (d) A superlattice DF-TEM image, taken using a S_3 spot (blue-dot circled), shows the rest of domain walls. Octahedral tilting directions in real space are shown in the up-right corner. (e) A high-angle annular dark-field image of one domain wall acquired along $[110]_T$. The superimposed structural model corresponds to one projected unit cell. Ca/Sr, Ti and Sr cations are shown with blue, green and grey spheres, respectively. The unit cells can be determined with the brackets 'l' or 'r' geometry of cation displacements. The number of brackets between two highlighted unit cells is an odd number, evidencing a π phase shift and the existence of an APB. A less distortion is evident in the yellow-shaded APB region.

cation ordering is also confirmed from the observation of a brighter contrast of perovskite layers than that of rock-salt layers (Figure 3e). The observation of eight-state vortex-antivortex defects composed of T' and O' state suggests an X_3^- mode-driven phase transition.

Figure 4a summarises two types of Z_4 vortices (types i and ii) and two types of Z_4 antivortices (types iii and iv) observed in Figure 3a. Topological charge or winding number ' n ' is assigned when vectors rotate clockwise by $2\pi n$ along the clockwise direction around a core. Then, the topological charges of types i , ii , iii and iv topological defects are $+1$, $+1$, -1 and -1 , respectively, which indicates that types i and ii are vortices and types iii and iv are antivortices. We emphasise that vectors in a type i topological defect rotate opposite to those in a type ii topological defect, but they have the same topological charge, so both of them are vortices. A Z_4 vortex is always surrounded by antivortices and vice versa; for example, the vortex ' i ' in Figure 3a is connected to the antivortex ' iii ' and the antivortex ' iv '. Figure 4b illustrates the local structure around a type i Z_4 vortex (Figure 4a) with red-circled ①, ②, ③ and ④ domains, and domain walls of DW①② (blue-broken lines), DW①④ (light-blue-broken), DW③④ (blue) and DW②③ (light blue). By averaging the structure of neighbouring domains, DW①② and DW③④ share the same $[110]_T$ -tilting axis, but are different in the origin by a half of the unit cell. Similarly, DW②③ and DW①④ have the same tilting axis, which is consistent with the extinction rules observed in Figures 3c and d. On the other hand, a geometric frustration of oxygen octahedral distortions between two antiphase domains occurs likely in DW①③ (Figure 4c), leading to an undistorted domain wall in a T structure-like high-symmetric state. The absence of Z_3 vortices where three types of domain walls merge at one point reveals the nonexistence of $(\frac{1}{2}, \frac{1}{2}, 0)$ -type APB such as DW①③, which, in turn, indicates a much higher energy associated with APBs.

DISCUSSION

The T' state showing Z_4 vortices occurs in a narrow compositional range of $(\text{Ca,Sr})_3\text{Ti}_2\text{O}_7$. When octahedral rotation (thus, hybrid improper ferroelectricity) is suppressed by chemical doping/ionic ordering, Z_4 vortices emerge in the narrow compositional range, where domain and domain walls are intricately intertwined with the T' and O' states, arising from the active X_3^- mode. A full isotropy subgroup analysis²⁹ further implies a missing intermediate orthorhombic $Pnmm$ state, representing order parameter direction (a, b) , which is a subgroup of both of the T' and O' states, and is expected by symmetry to link domain and domain walls. A similar rule has been also applied to topological Z_6 vortices in hexagonal system, $h\text{-In}(\text{Mn}_{0.9}\text{Ga}_{0.1})\text{O}_3$, where the K_3 mode is characterised by trimerising tilts of the MnO_5 trigonal bipyramids. Three low-symmetry possibilities derived from the parent $P6_3/mmc$ structure are allowed by the K_3 mode, corresponding to 12 phases of domains and domain walls and an intermediate state link them.³¹ Real-space topological defects can be well classified in terms of one specific lattice mode, which leads to a valid physical insight into the phase transition and serves as a platform to uncover additional hidden symmetry and new topological defects. In addition, our new discovery of ' $Z_2 \times Z_2$ domains with Z_4 vortices' unveils that there can be a lot more than just the topological defects ($Z_2 \times Z_3$ domains with Z_6 vortices) in hexagonal rare-earth manganites, which has been extensively investigated since the initial discovery in 2010 (ref. 32). Z_6 vortices observed in improper ferroelectric rare-earth manganites^{31,32} and skyrmions in low-symmetry magnets³³ have provided a new paradigm in the quest for mesoscopic self-organised structures with non-trivial topology, which can have novel functionalities. Emphasise that the octahedral distortions in the T' state is also analogous to that observed in the so-called low-temperature

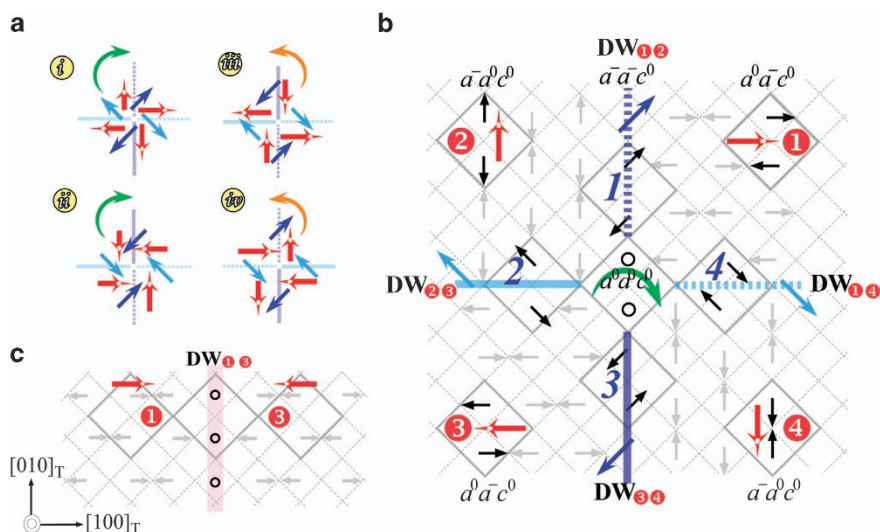


Figure 4. (a) Schematics illustrate the oxygen octahedral distortion configurations at domains and domain walls of Z_4 vortex–antivortex defects shown in Figure 3a. Red arrows for four domains show apical oxygen tilts along the $\langle 100 \rangle_T$ directions. Blue and light-blue bold lines represent two types of domain walls originated from two different tilting axes, and solid and broken lines are related by a translational symmetry. Yellow-circled types *i* and *ii* are Z_4 vortices and types *iii* and *iv* are Z_4 antivortices. (b) Local oxygen distortions of a type *i* Z_4 vortex with four domains (red-circled 1–4) and four domain walls (blue 1–4) in the ab plane. The local apical oxygen distortions in each domain and domain wall are shown by small gray and black arrows. The gray solid squares outline the $\sqrt{2} \times \sqrt{2}$ supercell with the T' ($P4_2/mnm$) symmetry inside domains and with the O' ($Amam$) symmetry at domain walls. A frustration of oxygen octahedral tilts among four domains suggests an un-distorted structure (open circles) for the Z_4 vortex core. The Glazer notations label the dominant tilting modes at the corresponding locations. (c) A schematic of the domain wall between two antiphase domains, e.g., DW₁₃ between domain 1 and 3. The open circles indicate the ideal position of oxygens of the T state.

tetragonal state of high- T_c superconducting $\text{La}_{2-x}\text{Sr}_x\text{CuO}_4$, in which the CuO_6 octahedra also tilt along the $\langle 100 \rangle_T$ directions^{12,13} and are governed by the X_3^+ lattice mode.³⁴ We also note that the T' structure has been reported in other bi-layered perovskite magnets such as $\text{Sr}_2(\text{Ho,Y})\text{Mn}_2\text{O}_7$ (ref. 35) and $\text{Tb}_2\text{Sr}(\text{Fe,Co})_2\text{O}_7$ (refs 36–38), and magnetism in (layered) perovskites tends to be strongly coupled with structural distortions, so this unique domain topology may not be limited to structural domains and domain walls in $(\text{Ca,Sr})_3\text{Ti}_2\text{O}_7$. Our work should initiate further exploration of new types of topological defects.

MATERIALS AND METHODS

Eleven high-quality polycrystalline specimens of $\text{Ca}_{3-x}\text{Sr}_x\text{Ti}_2\text{O}_7$ ($x=0, 0.3, 0.5, 0.6, 0.8, 0.85, 0.9, 1, 1.5, 2$ and 3) were prepared using a solid-state reaction method. Stoichiometric mixtures of CaCO_3 (Alfa Aesar 99.95%), SrCO_3 (Alfa Aesar 99.99%) and TiO_2 (Alfa Aesar Puratronic 99.995%) powders were ground, pelletised and then sintered at 1,550–1,660 °C for 30 h. In the range of $1.1 \leq x < 1.5$, we found a triple-layered $\text{A}_4\text{B}_3\text{O}_{10}$ phase is more stable and favoured than the bi-layered $\text{A}_3\text{B}_2\text{O}_7$ phase. The powder specimens for acquiring synchrotron X-ray powder diffraction data were sealed in 0.2-mm-diameter capillary quartz tubes. All synchrotron X-ray experiments were performed on beamline BL01C2 at the National Synchrotron Radiation Research Center, Taiwan. The powder diffraction patterns were acquired using a collimated synchrotron-radiation beam with the wavelength of 0.688 Å (18 KeV). Powdered sample were loaded into a 0.2-mm capillary for uniform absorption and faster rotation during data collection. The general structure analysis program using the Rietveld method with a pseudo-Voigt profile function was exploited to analyse the X-ray powder diffraction data. Specimens for transmission electron microscope (TEM) studies were prepared by mechanical polishing, followed by Ar-ion milling, and studied using a JEOL-2010F TEM at Rutgers University, NJ. We observed Z_4 vortex domains with superlattice DF-TEM imaging taking (1) $S_1 = \frac{1}{2}(130)_T = (120)_{\text{orth}}$, (2) $S_2 = \frac{1}{2}(020)_T = (110)_{\text{orth}}$ and (3) $S_3 = \frac{1}{2}(\bar{1}30)_T = (210)_{\text{orth}}$ spots. *In situ* heating TEM experiment was carried out using a JEOL-2000FX TEM with a high-temperature specimen holder at National Taiwan University in Taiwan. High-angle annular dark-field scanning TEM imaging with atomic-column

resolution was carried out using a JEOL-2100F microscope equipped with a spherical aberration Cs-corrector at National Taiwan University in Taiwan. High-angle annular dark-field images were acquired in the condition: 512×512 with 0.024 nm per pixel with collection angle between 80 and 210 mrad. For dielectric constant measurements, two electrodes were prepared using Au sputtering on polished specimens with a capacitor geometry, and an LCR metre at $f=44$ kHz was utilised.

Data availability

The authors declare that all source data supporting the findings of this study are available within the article and the file.

ACKNOWLEDGEMENTS

The work at Rutgers was funded by the Gordon and Betty Moore Foundation's EPIQS Initiative through Grant GBMF4413 to the Rutgers Center for Emergent Materials, and the work at Postech was supported by the Max Planck POSTECH/KOREA Research Initiative Program (grant no. 2011-0031558) through NRF of Korea funded by MSIP.

CONTRIBUTIONS

F.-T.H. and M.-W.C. conducted the (S)TEM experiments. B.G. and X.L. synthesised single crystals. J.W.K. and Y.W. performed the dielectric measurements. C.-K.C. and H.-S. S. acquired the synchrotron X-ray data. F.-T.H. and S.-W.C. wrote the paper. S.-W.C. initiated and supervised the research.

COMPETING INTERESTS

The authors declare no conflict of interest.

REFERENCES

1. Bednorz, J. G. & Müller, K. A. Perovskite-type oxides—the new approach to high- T_c superconductivity. *Rev. Mod. Phys.* **60**, 585–600 (1988).
2. Cheong, S.-W. & Mostovoy, M. Multiferroics: a magnetic twist for ferroelectricity. *Nat. Mater.* **6**, 13–20 (2007).

3. Von Hippel, A. Ferroelectricity, domain structure, and phase transitions of barium titanate. *Rev. Mod. Phys.* **22**, 221–246 (1950).
4. Salamon, M. B. & Jaime, M. The physics of manganites: Structure and transport. *Rev. Mod. Phys.* **73**, 583–628 (2001).
5. Haghir-Gosnet, A. M. & Renard, J. P. CMR manganites: physics, thin films and devices. *J. Phys. D Appl. Phys.* **36**, R127–R150 (2003).
6. Uehara, M., Mori, S., Chen, C. H. & Cheong, S. W. Percolative phase separation underlies colossal magnetoresistance in mixed-valent manganites. *Nature* **399**, 560–563 (1999).
7. Choi, T., Lee, S., Choi, Y. J., Kiryukhin, V. & Cheong, S. W. Switchable ferroelectric diode and photovoltaic effect in BiFeO₃. *Science* **324**, 63–66 (2009).
8. Yang, W. S., Noh, J. H., Jeon, N. J., Kim, Y. C. & Ryu, S. High-performance photovoltaic perovskite layers fabricated through intramolecular exchange. *Science* **348**, 1234–1237 (2015).
9. Kim, H. J. *et al.* High mobility in a stable transparent perovskite oxide. *Appl. Phys. Express* **5**, 061102 (2012).
10. Filip, M. R., Eperon, G. E., Snaith, H. J. & Giustino, F. Steric engineering of metal-halide perovskites with tunable optical band gaps. *Nat. Commun.* **5**, 5757 (2014).
11. Navrotsky, A. Energetics and crystal chemical systematics among ilmenite, lithium niobate, and perovskite structures. *Chem. Mater.* **10**, 2787–2793 (1998).
12. Zhu, Y., Moodenbaugh, A. R., Cai, Z. X., Taftø, J. & Suenaga, M. Tetragonal-orthorhombic structural modulation at low temperature in La_{2-x}Ba_xCuO₄. *Phys. Rev. Lett.* **73**, 3026–3029 (1994).
13. Chen, C. H., Cheong, S.-W., Werder, D. J. & Takagi, H. Microstructural changes induced by lattice instabilities in La_{2-x}Ba_xCuO₄ (x = 0.125) and Nd₂NiO₄. *Physica C* **206**, 183–194 (1993).
14. Sergienko, I. A. & Dagotto, E. Role of the Dzyaloshinskii-Moriya interaction in multiferroic perovskites. *Phys. Rev. B* **73**, 094434 (2006).
15. Reaney, I. M. & Woodward, D. I. Displacive phase transitions and intermediate structures in perovskites. *J. Am. Ceram. Soc.* **94**, 2242–2247 (2011).
16. Ahart, M. *et al.* Origin of morphotropic phase boundaries in ferroelectrics. *Nature* **451**, 545–548 (2008).
17. Millis, A. J. Lattice effects in magnetoresistive manganese perovskites. *Nature* **392**, 147–150 (1998).
18. Imada, M., Fujimori, A. & Tokura, Y. Metal-insulator transitions. *Rev. Mod. Phys.* **70**, 1039–1264 (1998).
19. Mulder, A. T., Benedek, N. A., Rondinelli, J. M. & Fennie, C. J. Turning ABO₃ antiferroelectrics into ferroelectrics: design rules for practical rotation-driven ferroelectricity in double perovskites and A₃B₂O₇ Ruddlesden-Popper compounds. *Adv. Funct. Mater.* **23**, 4810–4820 (2013).
20. Oh, Y. S., Luo, X., Huang, F.-T., Wang, Y. & Cheong, S.-W. Experimental demonstration of hybrid improper ferroelectricity and the presence of abundant charged walls in (Ca,Sr)₃Ti₂O₇ crystals. *Nat. Mater.* **14**, 407–413 (2015).
21. Benedek, N. A. & Fennie, C. J. Hybrid improper ferroelectricity: a mechanism for controllable polarization-magnetization coupling. *Phys. Rev. Lett.* **106**, 107204 (2011).
22. Huang, F.-T. *et al.* Domain topology and domain switching kinetics in a hybrid improper ferroelectric. *Nat. Commun.* **7**, 11602 (2016).
23. Harris, A. B. Symmetry analysis for the Ruddlesden-Popper systems Ca₃Mn₂O₇ and Ca₃Ti₂O₇. *Phys. Rev. B* **84**, 064116 (2011).
24. Glazer, A. M. The classification of tilted octahedra in perovskites. *Acta Cryst. B* **28**, 3384–3392 (1972).
25. Senn, M. S. *et al.* Symmetry switching of negative thermal expansion by chemical control. *J. Am. Chem. Soc.* **138**, 5479–5482 (2016).
26. Senn, M. S. *et al.* Negative thermal expansion in hybrid improper ferroelectric Ruddlesden-Popper perovskites by symmetry trapping. *Phys. Rev. Lett.* **114**, 035701 (2015).
27. Pitcher, M. J., Mandal, P., Dyer, M. S., Alaria, J. & Borisov, P. Tilt engineering of spontaneous polarization and magnetization above 300 K in a bulk layered perovskite. *Science* **347**, 420–424 (2015).
28. Chae, S. C. *et al.* Self-organization, condensation, and annihilation of topological vortices and antivortices in a multiferroic. *Proc. Natl Acad. Sci. USA* **107**, 21366–21370 (2010).
29. Stokes, H. T. & Hatch, D. M. *Isotropy Subgroup of the 230 Crystallographic Space Groups*. World Scientific: Singapore, (1988).
30. Jia, C.-L. *et al.* Atomic-scale study of electric dipoles near charged and uncharged domain walls in ferroelectric films. *Nat. Mater.* **7**, 57–61 (2008).
31. Huang, F.-T. *et al.* Duality of topological defects in hexagonal manganites. *Phys. Rev. Lett.* **113**, 267602 (2014).
32. Choi, T. *et al.* Insulating interlocked ferroelectric and structural antiphase domain walls in multiferroic YMnO₃. *Nat. Mater.* **9**, 253–258 (2010).
33. Yu, X. Z. *et al.* Real-space observation of a two-dimensional skyrmion crystal. *Nature* **465**, 901–904 (2010).
34. Balachandran, P. V., Puggioni, D. & Rondinelli, J. M. Crystal-chemistry guidelines for noncentrosymmetric A₂BO₄ Ruddlesden-Popper Oxides. *Inorg. Chem.* **53**, 336–348 (2014).
35. Battle, P. D., Millburn, J. E. & Rosseinsky, M. J. Neutron diffraction study of the structural and electronic properties of Sr₂HoMn₂O₇ and Sr₂YMn₂O₇. *Chem. Mater.* **9**, 3136–3143 (1997).
36. Sánchez-Andújar, M. & Señaris-Rodríguez, M. A. Cation ordering and electrical properties of the Ruddlesden-Popper Gd_{2-2x}Sr_{1+2x}Co₂O₇ compounds (x = 0 and 0.10). *Z. anorg. allg. Chem.* **633**, 1890–1896 (2007).
37. Hickey, P. J., Knee, C. S., Henry, P. F. & Weller, M. T. Spin-crossover structural transition in the layered perovskite Gd₂SrCo₂O₇. *Phys. Rev. B* **75**, 024113 (2007).
38. Samaras, D., Collomb, A. & Joubert, J. C. Determination des structures de deux ferrites mixtes nouveaux de formule BaLa₂Fe₂O₇ et SrTb₂Fe₂O₇. *J. Solid State Chem.* **7**, 337–348 (1973).



This work is licensed under a Creative Commons Attribution 4.0 International License. The images or other third party material in this article are included in the article's Creative Commons license, unless indicated otherwise in the credit line; if the material is not included under the Creative Commons license, users will need to obtain permission from the license holder to reproduce the material. To view a copy of this license, visit <http://creativecommons.org/licenses/by/4.0/>

© The Author(s) 2016

Supplementary Information accompanies the paper on the *npj Quantum Materials* website (<http://www.nature.com/npjquantmats>)